This manuscript is a preprint and has not been peer reviewed. The copyright holder has made the manuscript available under a Creative Commons Attribution 4.0 International (CC BY) license and consented to have it forwarded to EarthArXiv for public posting.

From individual gathers to source-composite inversion in active multichannel analysis of surface waves (MASW): A paired field comparison of 8kg hammer and gun acquisition protocols

Prince Larbi Akor[1*], Nelson Foli[2], Ruth Araba Tawiah Annan[3], Emmanuel Teye Mensah[4], Edmund Okoe Amartey[5], Essinam Aku Viotay[6], Naomi Tawiah Quarshie[7], Judith Tansi Addy[8] Jeffery Nelson[9], Emmanuel Kwame Nuamah[10]

[1-8]National Nuclear Research Institute, Ghana Atomic Energy Commission, Accra, Greater Accra, Ghana

[9,10]Department of Earth Science, University of Ghana

Abstract

In multichannel analysis of surface waves (MASW), the suitability of an active source is evaluated by its ability to generate coherent and continuous surface-wave dispersion over a usable frequency and wavelength range, as these characteristics influence the reliability of mode identification and the attainable depth of investigation. We present a hierarchical paired comparison of hammer and gun acquisition protocols using 13 matched source positions and identical 12-receiver geometry (5m spacing, 55m aperture and 30m nearest offset). All 26 SEG-2 gathers were processed individually using the same phase-shift imaging and automated ridge-extraction criteria, followed by independent manual fundamental-mode picking to verify the automatic interpretation before acceptance and inversion. The verified individual gathers were then combined through normalized common-offset trace stacking and normalized dispersion-image stacking for each source. Every gather yielded an accepted fundamental-mode path. At the individual-gather level, mean maximum usable wavelength was 30.14m for the hammer and 29.45m for the gun (gun minus hammer = −0.69m; 95% paired bootstrap interval −3.81 to 1.50m). The hammer contained a greater proportional 4.5–10Hz spectral fraction (0.967% versus 0.672%), but this exploratory contrast did not remain significant after Holm correction [14]. Source-composite curves spanned 21.0–46.0Hz for the hammer and 20.5–43.5Hz for the gun, with maximum wavelengths of 32.14 and 33.41m, respectively. The stacked gun-minus-hammer wavelength difference was 1.27m (paired spatial-bootstrap 95% interval −1.39 to 2.50m), equivalent to upper screening depths of 16.07 and 16.71m under a 0.5 wavelength convention. Fixed-layer conditional inversions produced overlapping shear-wave velocity

This manuscript is a preprint and has not been peer reviewed. The copyright holder has made the manuscript available under a Creative Commons Attribution 4.0 International (CC BY) license and consented to have it forwarded to EarthArXiv for public posting.

intervals in all four model layers; gun-minus-hammer differences ranged from −17.6 to +14.1m/s and all 95% intervals included zero. Agreement between independently extracted trace-stack and image-stack curves was 7.16m/s for the hammer and 4.15m/s for the gun. These results show that source ranking is endpoint and threshold dependent: the hammer supplied more relative low-frequency energy, whereas the gun stack gave a slightly longer wavelength, but neither a reliable depth advantage nor a distinct velocity structure was resolved. The proposed individual-to-stack consistency framework, strengthened by manual verification of automated modal picks, provides a reproducible way to prevent source-energy observations from becoming unsupported claims of deeper MASW investigation.

Keywords: Active MASW; Source comparison; Dispersion imaging; Stacking; Shear-wave velocity; Depth of investigation

1. Introduction

Multichannel analysis of surface waves (MASW) uses the frequency-dependent phase velocity of Rayleigh waves to infer near-surface shear-wave velocity structure. The method is attractive because acquisition is non-invasive, field deployment is rapid and shear-wave velocity is directly related to small-strain stiffness. A conventional workflow comprises multichannel acquisition, transformation to a dispersion-image domain, extraction of one or more modal curves and inversion for a layered velocity model [1,2,3]. Each stage introduces assumptions, and acquisition or modal-identification errors can propagate into apparently precise but poorly constrained profiles [4,5,6].

Active-source bandwidth interacts with site attenuation, source coupling, receiver characteristics, source offset and array aperture. Longer wavelengths are required for deeper sensitivity, while shorter wavelengths improve shallow resolution. A more energetic source may strengthen low-frequency motion, but energy is useful only if it forms a coherent, localized and physically plausible dispersion ridge [7,8,9]. Impact-plate material, repeated impacts, preprocessing and near-field effects can also change image quality [10,11]. The lowest frequency containing visible energy is therefore not necessarily the minimum usable dispersion frequency.

A second complication is scale. A single gather describes source performance at one location, whereas a moving-spread survey samples lateral variation in coupling and near-surface structure. Stacking can increase repeatability but can also blur true lateral changes. Comparing

This manuscript is a preprint and has not been peer reviewed. The copyright holder has made the manuscript available under a Creative Commons Attribution 4.0 International (CC BY) license and consented to have it forwarded to EarthArXiv for public posting.

sources only after stacking hides position-specific failures; comparing only individual gathers may mistake local variability for a source effect. A defensible comparison should therefore ask whether the source ranking persists across individual gathers, threshold choices, trace-domain stacks, dispersion-image stacks and inverse models.

Depth of investigation is equally easy to overstate. Wavelength is phase velocity divided by frequency, and sensitivity decays over a depth interval rather than terminating at a fixed boundary. Wavelength fractions are useful screening conventions, not proof that every model parameter is resolved. Non-uniqueness means that an inversion extended to 30 m does not demonstrate 30 m resolution [4,12]. Resolution claims should be constrained by the longest defensible wavelength and by uncertainty propagated through picking and inversion.

This study introduces an individual to composite source performance consistency test for 13 paired hammer and gun positions. The objectives are to: (1) process every gather with identical MASW criteria; (2) compare spectral content, phase coherence, ridge localization, usable bandwidth and maximum wavelength in a paired design; (3) extract the fundamental-mode dispersion path automatically and verify it independently by manual phase picking; (4) form independent trace-domain and dispersion-image composites for each source; (5) invert the final composite curves with uncertainty; and (6) determine whether an apparent source advantage survives changes in analytical scale, picking approach and quality threshold. The novelty lies in treating source performance as a hierarchy of evidence rather than as a single amplitude, frequency or inversion plot.

2. Materials and Methods

2.1 Survey Design and Paired Acquisition

The MASW field survey was carried out using SmartSeis seismograph system. At each source position, 4.5Hz 12 geophones were deployed at 5m spacing, producing a 55m active receiver aperture. The seismic source was positioned 30m from the nearest receiver. Each trace was recorded with 4,000 samples at a sampling interval of 0.0005s, corresponding to a 2.0 s record length and a sampling frequency of 2,000Hz. A fixed gain of 36dB was used during acquisition. For both source types, the source-receiver spread was advanced along the survey line in 5m increments from source coordinate 0 to 60m, giving 13 shot locations for each source. The

This manuscript is a preprint and has not been peer reviewed. The copyright holder has made the manuscript available under a Creative Commons Attribution 4.0 International (CC BY) license and consented to have it forwarded to EarthArXiv for public posting.

common rolling acquisition geometry and the hierarchical analysis sequence are illustrated in Fig 1, while the principal acquisition characteristics are summarized in Table 1.

Thirteen hammer shot gathers (records 301–313) and 13 gunshot gathers (records 401–413) were acquired. The two datasets were paired according to physical source coordinate so that records obtained at equivalent field positions were compared directly. The gun-source survey was acquired in the reverse direction along the line: the gun record at source coordinate 0 m corresponded to acquisition sequence 413, whereas the record at 60m corresponded to sequence 401. Pairing by source coordinate rather than record number therefore prevented reversal of the spatial correspondence between the two datasets. Multiple impacts or source activations were used at selected shot locations to improve signal quality. The number of recorded field stacks varied from 3 to 7 for the hammer and from 1 to 4 for the gun. Because the stack counts differed between source types, raw recorded amplitude was not interpreted directly as a measure of relative source energy.

Fig 1. Common rolling acquisition geometry and hierarchical analysis workflow. Each paired position retained a 30 m nearest offset, 5m receiver spacing and 55m aperture; source performance was evaluated at waveform, dispersion, stack and inversion levels.

Table 1. Acquisition characteristics

Parameter	Hammer	Gun	Interpretation
Matched positions	13	13	Position defined by source coordinate
Channels per gather	12	12	Receiver count
Samples per channel	4,000	4,000	2.0 s record
Sample interval	0.0005 s	0.0005 s	2,000 Hz sampling
Receiver spacing	5 m	5 m	55 m aperture
Nearest source offset	30 m	30 m	Distance from source to 1st receiver
Header stack range	3–7	1–4	Raw amplitude not directly comparable
Accepted individual curves	13/13	13/13	Common primary criterion

2.2 Data Audit and Preprocessing

We developed a custom processing workflow to audit and preprocess the SEG-2 MASW records. The code directly read the SEG-2 trace descriptors and 32-bit floating-point seismic samples and extracted the principal acquisition parameters required for quality control. These included the number of traces, number of samples per trace, sampling interval, source and

This manuscript is a preprint and has not been peer reviewed. The copyright holder has made the manuscript available under a Creative Commons Attribution 4.0 International (CC BY) license and consented to have it forwarded to EarthArXiv for public posting.

receiver coordinates, fixed gain, line identifier, acquisition sequence and recorded stack count. SHA-256 hashes were also generated to provide a reproducible record of the datasets used in the analysis. All 26 shot gathers satisfied the structural, temporal and geometric consistency checks and were retained for subsequent processing.

Before dispersion analysis, we removed the mean value of each seismic trace to suppress the zero-frequency component. A Hann window was applied only when computing record-level power spectra and was not applied to the records used for phase-shift dispersion imaging. Spectral power was evaluated within the frequency range relevant to the 4.5 Hz geophones, and the proportion of power contained within the 4.5–10, 10–20, 20–40 and 40–80 Hz bands was calculated for comparison between the two seismic sources. We performed dispersion imaging on the demeaned full-length records using a custom implementation of the multichannel phase-shift method commonly used in MASW processing. The numerical formulation followed the phase-shift imaging principles described by Park et al. (1998, 1999) [13,1] and the computational approach implemented in MASWavesPy. Our code therefore reproduced the established MASW procedure of transforming multichannel surface-wave records from the time-offset domain into the frequency-phase-velocity domain by compensating the Fourier-domain phase of each trace for a range of trial phase velocities and coherently summing the phase-aligned contributions across the receiver array. Where multiple records or stacks were combined, we normalized record amplitudes before summation so that differences in source amplitude, acquisition gain and number of field stacks did not allow a limited number of records to dominate the resulting dispersion image.

2.3 Dispersion Imaging and Path Extraction

We developed an automated dispersion-ridge extraction routine to provide a consistent and reproducible first-pass identification of the fundamental-mode Rayleigh-wave trend from each calculated dispersion image. The underlying dispersion calculation retained the phase-shift formulation used in MASWavesPy, while the ridge-tracking and acceptance criteria were implemented specifically for this study. For each frequency, we projected the complex Fourier phase of the receiver traces over a prescribed range of trial phase velocities and coherently summed the responses. The resulting normalized dispersion-energy function was evaluated over phase velocities from 50 to 2,000 m/s at 5 m/s intervals and frequencies from 4.5 to 60 Hz at 0.5 Hz intervals. Automated ridge tracking was restricted to a phase-velocity range of 250–1, 200 m/s to limit the search to the range considered physically plausible for the

This manuscript is a preprint and has not been peer reviewed. The copyright holder has made the manuscript available under a Creative Commons Attribution 4.0 International (CC BY) license and consented to have it forwarded to EarthArXiv for public posting.

investigated near-surface materials. Rather than independently selecting the maximum-amplitude point at every frequency, we designed the algorithm to search for a continuous dispersion trajectory. The objective function favoured strong local maxima while penalizing abrupt phase-velocity changes between neighbouring frequency bins, thereby reducing the tendency of the automatic picker to jump between neighbouring modes, sidelobes or isolated high-amplitude artefacts.

We incorporated additional acceptance criteria into the code to distinguish coherent dispersion energy from poorly resolved spectral maxima. A candidate dispersion point was accepted when the normalized peak coherence was at least 0.55 and the ridge-sharpness ratio was at least 1.60. Ridge sharpness was defined as the amplitude of the selected dispersion peak divided by a robust estimate of the off-ridge background amplitude at the same frequency. The corresponding Rayleigh wavelength, calculated as $\lambda = v/f$, was required to lie between 10 and 55m, and a valid automated ridge was required to contain at least four consecutive accepted frequency bins.

In addition to automatic ridge extraction, we manually picked the fundamental-mode dispersion trend on every individual and source-composite dispersion image. Manual picking was used primarily as an independent quality-control procedure to assess whether the automatically extracted path followed the same coherent fundamental-mode ridge identified by visual interpretation. The manual review considered ridge continuity, peak localization, physically plausible phase-velocity variation and possible interference from higher modes, sidelobes or body-wave energy. An automatically extracted path was retained for quantitative analysis only when its modal interpretation was consistent with the manual pick; where disagreement occurred, the dispersion image and automated path were re-examined before a final accepted curve was defined. This combined automatic–manual procedure preserved the reproducibility of algorithmic picking while retaining the expert quality control recommended for surface-wave dispersion interpretation [5,6].

We used the longest accepted wavelength, $\lambda_{max} = v/f$, as the principal parameter for comparing the low-frequency and long-wavelength performance of the hammer and gun sources. Because the relationship between wavelength and investigation depth is approximate and depends on the subsurface velocity structure and modal sensitivity, we expressed potential depth support as approximately $0.3\lambda_{max}$ to $0.5\lambda_{max}$ rather than treating it as a fixed penetration-depth boundary.

This manuscript is a preprint and has not been peer reviewed. The copyright holder has made the manuscript available under a Creative Commons Attribution 4.0 International (CC BY) license and consented to have it forwarded to EarthArXiv for public posting.

2.4 Individual Gather Inversion

Every accepted individual curve was fitted with the same deliberately low-parameter fundamental-mode Rayleigh-wave model: finite layers at 0–2, 2–5 and 5–9m over a half-space. Shear-wave velocities were estimated while layer thicknesses were fixed. Compressional velocity was set to √3 times shear-wave velocity and density to 1,800, 1,900, 2,000 and 2,100 kg/m³ from shallow to deep. Forward Rayleigh-wave dispersion curves were calculated using the disba Python library, which provides computationally efficient surface-wave dispersion modelling for horizontally layered media. A global search followed by bounded least-squares refinement minimized coherence-weighted phase-velocity residuals. These models are conditional summaries for source comparison, not unique geologic solutions.

2.5 Source Composites

Two independent composites were generated for each source. First, traces were grouped by common receiver offset, normalized within each gather and median-combined over the 13 positions; the resulting 12-trace source gather was imaged and its fundamental mode was extracted automatically and checked manually. Second, each individual phase-shift image was normalized and the 13 images were averaged before automatic path extraction and manual verification. The trace-stack curve was used for the final conditional inversion, while the median absolute phase-velocity difference between trace-stack and image-stack curves quantified route consistency. Because the survey rolled along the line, the composites represent source-wide average response rather than a local 1-D sounding at one coordinate.

2.6 Uncertainty and Paired Inference

Continuous individual-gather outcomes were compared as gun minus hammer. Mean paired differences received percentile confidence intervals from paired bootstrap resampling of the 13 spatial positions and two-sided exact sign-flip tests. Holm adjustment was applied within a prespecified exploratory family of 14 waveform, spectral and image-quality outcomes. Dispersion endpoints were kept separate because threshold selection induces censoring and dependence.

Composite uncertainty used 200 paired spatial-bootstrap replicates [15]. Each replicate resampled matched positions with replacement, rebuilt both source composites, perturbed the curve using its estimated ridge width and repeated the inversion. The same resampled positions were used for both sources, preserving the paired design. Reported velocity intervals are

This manuscript is a preprint and has not been peer reviewed. The copyright holder has made the manuscript available under a Creative Commons Attribution 4.0 International (CC BY) license and consented to have it forwarded to EarthArXiv for public posting.

conditional on the selected fundamental mode, fixed layer boundaries, Vp/Vs ratio, densities and perturbation model; they do not include full structural non-uniqueness.

3. Results

3.1 File Integrity, Geometry and Individual Retrieval

All 26 files contained 12 complete, equal-length traces and identical sampling and offset geometry. No shot was excluded. The reversed gun acquisition order was resolved from source coordinates and acquisition sequence values, producing 13 coordinate-matched pairs. Automatic ridge extraction produced a candidate fundamental-mode path for every hammer and gun gather. Each candidate was subsequently checked by independent manual phase picking, and only the manually verified path was carried forward to endpoint calculation and inversion. All 26 gathers satisfied the common acceptance criteria

3.2 Paired Waveform and Dispersion-image Performance

Raw global record RMS averaged 2,950 for the hammer and 2,690 for the gun, but the paired interval included zero and raw amplitude is confounded by unequal header stack counts. The hammer showed more proportional 4.5–10Hz power: 0.967% versus 0.672%, a gun-minus-hammer difference of −0.295 percentage points (95% interval −0.487 to −0.102; unadjusted p = 0.0134). Gun coherence was higher at 10–20Hz and hammer sharpness was higher in that band, but none of the 14 exploratory quality outcomes met the 0.05 family-wise threshold after Holm adjustment. In the primary 20–40 Hz band, mean coherence and sharpness were almost identical between sources. The principal paired waveform and dispersion-image outcomes are summarized in Table 2, and the position-level gun-minus-hammer differences are illustrated in Fig 2.

Table 2 Selected paired outcomes. Intervals are paired bootstrap intervals. Holm p applies to the 14 outcome exploratory quality family

Outcomes	Hammer	Gun	Difference	95% Interval	Exact p	Holm p
Record RMS	2950	2690	-261	-859 to 280	0.4255	1.0000
Dominant frequency (Hz)	41.54	39.46	-2.08	-6.38 to 1.23	0.3867	1.0000
4.5–10 Hz spectral fraction (%)	0.9672	0.6719	-0.2953	-0.4872 to -0.1022	0.0134	0.1611
10–20 Hz coherence	0.730	0.843	0.112	0.054 to 0.168	0.0049	0.0635

This manuscript is a preprint and has not been peer reviewed. The copyright holder has made the manuscript available under a Creative Commons Attribution 4.0 International (CC BY) license and consented to have it forwarded to EarthArXiv for public posting.

20–40 Hz coherence	0.885	0.887	0.003	-0.004 to 0.010	0.4910	1.0000
10–20 Hz sharpness	1.434	1.282	-0.151	-0.230 to -0.072	0.0044	0.0615
20–40 Hz sharpness	4.028	4.077	0.049	-0.039 to 0.133	0.3035	1.0000
Minimum usable frequency (Hz)	22.65	23.00	0.35	-1.31 to 2.27	0.6719	—
Maximum wavelength (m)	30.14	29.45	-0.69	-3.81 to 1.50	0.8323	—
Upper depth screen, 0.5λ (m)	15.07	14.73	-0.34	-1.90 to 0.72	0.8323	—

Fig 2. Paired source differences in selected spectral and dispersion-image metrics. Points show position-level gun-minus-hammer differences; summary markers and intervals quantify the paired mean.

3.3 Individual Dispersion Curves and Inversions

The dispersion images and accepted fundamental-mode phase-velocity picks for all 13 hammer gathers are presented in Fig 3, while the corresponding results for the 13 gun gathers are shown in Fig 4. Automatic ridge extraction was applied consistently to all records, followed by independent manual phase picking to verify the continuity and modal identity of the automatically selected fundamental-mode trends. The close correspondence between the automated and manually verified trajectories provided an additional quality-control check before the dispersion curves were used for wavelength analysis and inversion

The 26 accepted and manually verified fundamental-mode paths were supported mainly between approximately 18 and 49 Hz. Across positions, mean minimum usable frequency was 22.65Hz for hammer gathers and 23.00Hz for gun gathers. Mean maximum wavelength was 30.14 and 29.45m, respectively, corresponding to mean upper screening depths of 15.07 and 14.73 m. The paired differences in minimum frequency, wavelength and screening depth all included zero. The mean automatically evaluated picked-ridge coherence was 0.857 for hammer gathers and 0.856 for gun gathers; mean sharpness was 4.24 and 4.35. Manual inspection confirmed that the accepted automated trajectories followed the visually identifiable fundamental-mode ridges used for interpretation. The accepted dispersion endpoints for all matched positions are listed in Table 3, while their position-by-position variation and conditional inversion performance are summarized in Fig 5.

This manuscript is a preprint and has not been peer reviewed. The copyright holder has made the manuscript available under a Creative Commons Attribution 4.0 International (CC BY) license and consented to have it forwarded to EarthArXiv for public posting.

Fig 3. Phase-shift dispersion images for the 13 hammer-source shot gathers. The thin white line represents the automatically extracted dispersion ridge, while the solid line represents the manually verified fundamental mode Rayleigh-wave phase-velocity path.

Fig 4. Phase-shift dispersion images for the 13 gun-source shot gathers. The thin white line represents the automatically extracted dispersion ridge, while the solid line represents the manually verified fundamental mode Rayleigh-wave phase-velocity path.

Table 3. Individual accepted dispersion endpoints by matched source position. Depth of Investigation (D) is the conservative upper screening depth 0.5λmax.

Position	Hammer fmin (Hz)	Hammer λmax (m)	Hammer D (m)	Gun fmin (Hz)	Gun λmax (m)	Gun D (m)
1	18.0	36.67	18.33	18.5	35.41	17.70
2	19.0	35.00	17.50	18.0	36.94	18.47
3	19.5	34.36	17.18	19.0	35.00	17.50
4	19.5	34.10	17.05	19.5	34.87	17.44
5	20.0	34.00	17.00	20.0	34.50	17.25
6	20.0	34.75	17.38	20.0	34.50	17.25
7	22.0	31.59	15.80	21.5	33.02	16.51
8	23.0	29.57	14.78	23.5	28.72	14.36
9	25.0	26.60	13.30	26.0	25.58	12.79
10	27.0	22.04	11.02	28.5	21.40	10.70
11	25.0	25.60	12.80	25.0	25.80	12.90
12	36.5	12.33	6.16	30.0	18.50	9.25
13	20.0	35.25	17.62	29.5	18.64	9.32

Fig 5. Position-by-position summaries of usable dispersion endpoints and conditional inversion fit. Connecting lines emphasize the paired spatial design rather than temporal acquisition order.

This manuscript is a preprint and has not been peer reviewed. The copyright holder has made the manuscript available under a Creative Commons Attribution 4.0 International (CC BY) license and consented to have it forwarded to EarthArXiv for public posting.

3.4 Source-composite Dispersion

The normalized hammer trace stack yielded a 21.0–46.0 Hz curve with λmax = 32.14 m. The gun stack yielded a 20.5–43.5 Hz curve with λmax = 33.41 m. The gun therefore appeared 1.27 m longer in the final stacks, but the paired spatial-bootstrap interval was −1.39 to 2.50 m. The corresponding upper depth-screening values were 16.07 and 16.71 m, a difference of 0.64 m with interval −0.69 to 1.25 m. The source ranking thus changed from a small hammer advantage in the mean individual curves to a small gun advantage in the composites, with neither contrast resolved from zero.

Independent processing routes gave similar composite curves, and manual picking confirmed the same fundamental-mode trends selected by the automated procedure. Median absolute phase-velocity difference between the trace-stack and mean-image-stack curves was 7.16 m/s for the hammer and 4.15 m/s for the gun. The gun composite had marginally higher mean coherence and sharpness, but the differences were small relative to within-source and picking uncertainty. The final source-composite dispersion and inversion diagnostics are summarized in Table 4, and the trace-stack and image-stack results for both sources are shown in Fig 6.

Table 4. Final source-composite dispersion and inversion diagnostics.

Source	Shots	Usable f (Hz)	λmax (m)	Depth screen (m)	Coherence	Sharpness	Route MAD (m/s)	Fit MAPE (%)
Hammer	13	21.0–46.0	32.14	9.64–16.07	0.792	3.87	7.16	1.44
Gun	13	20.5–43.5	33.41	10.02–16.71	0.814	3.97	4.15	1.56

Fig 6. Source-composite results from normalized common-offset trace stacking and normalized dispersion-image stacking. Automated fundamental-mode paths were independently checked by manual phase picking; agreement of the two stacking routes provides additional processing consistency checks

3.5 Final Conditional Inversions

Both composite inversions show increasing Vs with depth under the common fixed-layer parameterization. Hammer Vs was 426, 526 and 646 m/s in the three finite layers, with an 815 m/s half-space. Gun Vs was 409, 524 and 653 m/s, with an 829 m/s half-space. Paired

This manuscript is a preprint and has not been peer reviewed. The copyright holder has made the manuscript available under a Creative Commons Attribution 4.0 International (CC BY) license and consented to have it forwarded to EarthArXiv for public posting.

composite differences were −17.6, −1.9, +7.5 and +14.1 m/s; every 95% interval included zero. The results therefore do not support source-dependent velocity structures at this site. The resulting source-composite layer velocities and their paired uncertainty intervals are reported in Table 5. The observed composite dispersion curves, forward-model fits and conditional layered Vs models are shown in Fig 7, while the distributions of all individual conditional Vs profiles are presented in Fig 8.

The half-space velocity affects the lowest-frequency part of the measured curve, but it must not be read as a fully resolved value to arbitrary depth. The data-supported upper screening depth is approximately 16–17 m. A displayed model extending to 30 m would be an extrapolation of the half-space assumption, not a 30 m resolved inversion.

Table 5. Final source-composite conditional Vs models. Parentheses give within-source 95% bootstrap intervals; differences and intervals are gun minus hammer.

Layer (m)	Hammer Vs (m/s)	Gun Vs (m/s)	Difference (m/s)	95% paired interval (m/s)
0–2	426.2 (346.8–477.2)	408.6 (317.4–447.7)	-17.6	-119.4 to 79.4
2–5	526.3 (486.9–587.8)	524.4 (475.9–584.7)	-1.9	-83.6 to 82.0
5–9	645.8 (608.7–723.2)	653.3 (625.5–742.7)	7.5	-73.0 to 95.7
>9 half-space	815.1 (734.6–866.4)	829.2 (787.2–897.9)	14.1	-41.0 to 123.1

Fig 7. Final source-composite dispersion fits and conditional layered Vs models. Shaded bands summarize paired spatial-bootstrap and curve-perturbation uncertainty. The horizontal depth marker shows the wavelength-based interpretation limit rather than plotting limit.

Fig 8. All individual conditional Vs profiles and their source-wise distributions. Similar profiles reflect both the paired geology and the common low-parameter inversion

This manuscript is a preprint and has not been peer reviewed. The copyright holder has made the manuscript available under a Creative Commons Attribution 4.0 International (CC BY) license and consented to have it forwarded to EarthArXiv for public posting.

4. Discussion

4.1 Source Performance Depends on the Endpoint

The paired experiment does not yield one universal winner. Hammer gathers contained a larger fraction of 4.5–10 Hz power, but their mean individual maximum wavelength was only 0.69 m longer than that of gun gathers, with wide paired uncertainty. After source-wide stacking, the ranking reversed and the gun curve was 1.27 m longer. Both estimates were small and included zero. A simple conclusion such as ‘the source with more low-frequency energy investigates deeper’ would therefore be contradicted by the dispersion endpoints themselves.

This distinction is physically reasonable. Spectral power measures how much energy occupies a band; dispersion usability requires consistent phase across the receiver array, adequate peak localization and continuity of a plausible mode. The hammer may generate proportionally more low-frequency motion without producing a more stable low-frequency ridge. Conversely, the gun may produce a marginally more coherent composite through repeated spatial consistency even when its normalized low-frequency power is lower.

4.2 Why Individual and Stacked Rankings can Differ

A mean of individual λmax values weights each position equally after a hard endpoint decision. The trace composite instead averages normalized waveforms before imaging, so phase-stable energy repeated across the line is reinforced and inconsistent energy is suppressed. The image composite similarly rewards repeatable maxima. Differences between the two scales need not indicate an error; they reveal whether a source effect is local or spatially persistent. Here, the rank reversal and overlapping intervals show that the apparent advantage is not robust enough to support an operational depth claim.

Threshold sensitivity leads to the same conclusion. Across coherence thresholds of 0.50–0.65 and sharpness thresholds of 1.4–2.0, all 26 gathers remained accepted, but the gun-minus-hammer mean λmax contrast changed sign. Retrieval success was robust, while fine source ranking was not. This is an important distinction for field-method publications: stable acceptability can coexist with unstable superiority.

This manuscript is a preprint and has not been peer reviewed. The copyright holder has made the manuscript available under a Creative Commons Attribution 4.0 International (CC BY) license and consented to have it forwarded to EarthArXiv for public posting.

4.3 What the Inversions do and do not show

The two source-composite models show the same broad stiffness increase with depth and statistically overlapping conditional layer velocities. Since both sources sampled the same rolling profile, agreement is expected if source treatment and modal identification are consistent. The agreement between automated and manual phase picking, together with the similarity between the two composite-processing routes, provides a useful internal quality-control check. It is not, however, an independent validation of the layer boundaries or a proof of geologic uniqueness.

The usable longest wavelengths, about 32–33 m, support a screening depth of roughly 10–17 m under 0.3–0.5λ conventions. Below this range the plotted half-space is weakly constrained and increasingly assumption-controlled. We therefore avoided a 30 m inversion claim. Deeper characterization would require longer usable wavelengths, a larger aperture and/or complementary passive surface waves, refraction, borehole or other constraints.

4.4 Methodological Contribution and Field Implications

The principal contribution is a reproducible source-performance hierarchy: verify provenance and pairing; analyse every gather; distinguish energy from ridge quality; extract the dispersion trajectory automatically; independently verify the fundamental mode by manual phase picking; test threshold sensitivity; construct both trace and image composites; invert with common low complexity; and propagate paired spatial and picking uncertainty. The hierarchy makes it harder for attractive dispersion plots or smooth Vs curves to outrun the data. It also turns a nuanced negative result into a useful survey-design result: under this geometry and site condition, both protocols were adequate, and source choice should be based on logistics, safety, repeatability and required bandwidth rather than a claimed depth advantage.

For practice, the 30 m nearest offset was workable in this dataset because all gathers produced continuous accepted paths and the two stack routes agreed closely. That observation is site and bandwidth specific, not a universal endorsement of the offset. Future source trials should preserve matched geometry, log impact and stack definitions explicitly, and predefine quality and wavelength criteria before comparing sources.

This manuscript is a preprint and has not been peer reviewed. The copyright holder has made the manuscript available under a Creative Commons Attribution 4.0 International (CC BY) license and consented to have it forwarded to EarthArXiv for public posting.

5. Conclusion

A complete paired analysis of 13 hammer and 13 gun MASW gathers showed that both active sources produced usable and internally consistent fundamental-mode Rayleigh-wave dispersion under the tested field geometry and processing conditions. All 26 gathers yielded accepted dispersion paths, and the automatically extracted ridges were independently checked by manual phase picking to confirm modal continuity and the correctness of the automated selections. Neither source exhibited a failure in fundamental-mode retrieval.

The hammer records contained a higher proportional contribution of spectral energy in the 4.5–10 Hz band, but this did not result in a consistently longer usable dispersion curve or greater wavelength-supported depth. At the individual-gather level, the mean maximum usable wavelength slightly favoured the hammer source, whereas the source-composite analysis slightly favoured the gun source. These differences were small, their uncertainty intervals included zero, and the relative ranking changed with the applied quality thresholds.

The final source-composite dispersion curves produced wavelength-based screening depths of approximately 16.1 m for the hammer and 16.7 m for the gun using the adopted $0.5\lambda_{max}$ criterion. These results indicate that the measured dispersion data provide comparable depth support for the two sources and do not justify interpreting a 30 m velocity model as fully resolved by the available surface-wave wavelengths.

The final conditional Vs models from the two sources were also closely comparable. Shear-wave velocities in all model layers overlapped within the paired uncertainty intervals, indicating that the hammer and gun sources recovered essentially the same subsurface velocity structure under the adopted inversion parameterization. Under the acquisition conditions used in this study, both sources were therefore suitable for MASW investigation, with neither showing a statistically defensible advantage in dispersion resolution, maximum usable wavelength, depth of investigation, or recovered Vs structure.

Overall, the study shows that reliable comparison of active MASW sources requires consistent evaluation across individual gathers, automated dispersion extraction, independent manual phase verification, quality-threshold testing, source stacking, and inversion. The combined results provide a reproducible basis for assessing source performance from the quality and stability of the recovered dispersion information and the consistency of the resulting shear-wave velocity models.

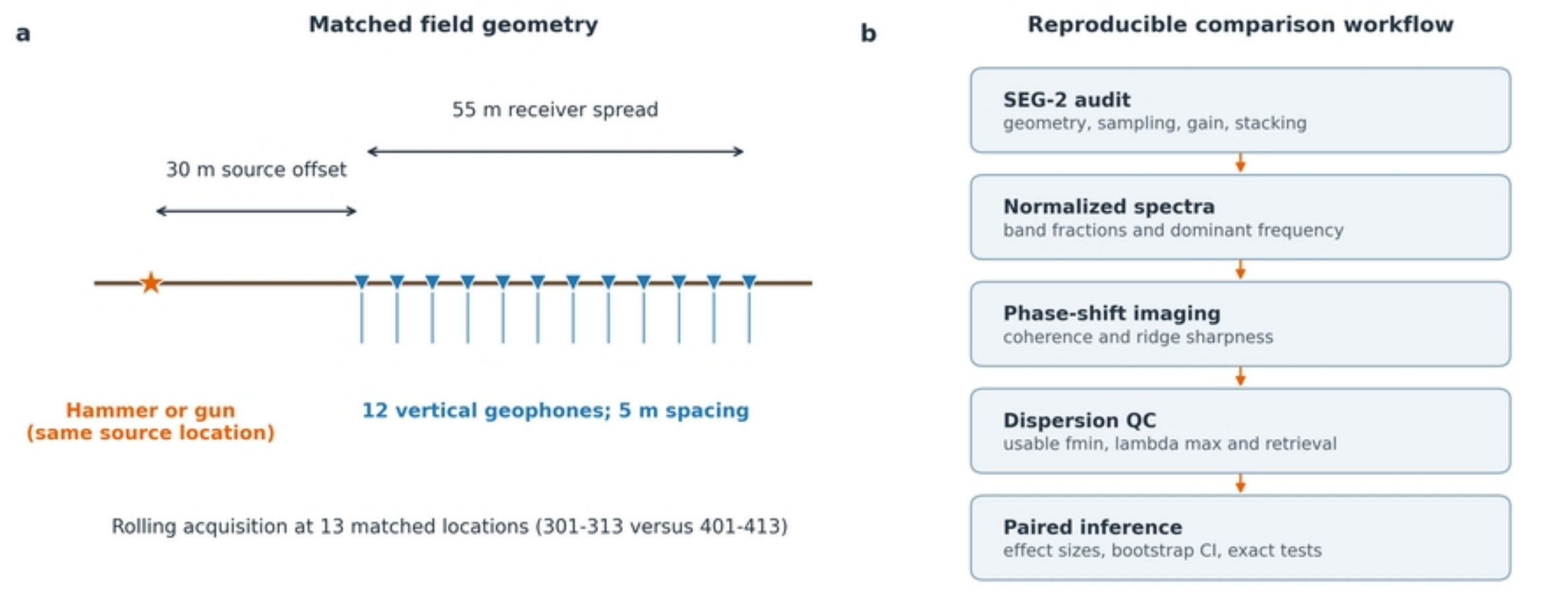
This manuscript is a preprint and has not been peer reviewed. The copyright holder has made the manuscript available under a Creative Commons Attribution 4.0 International (CC BY) license and consented to have it forwarded to EarthArXiv for public posting.

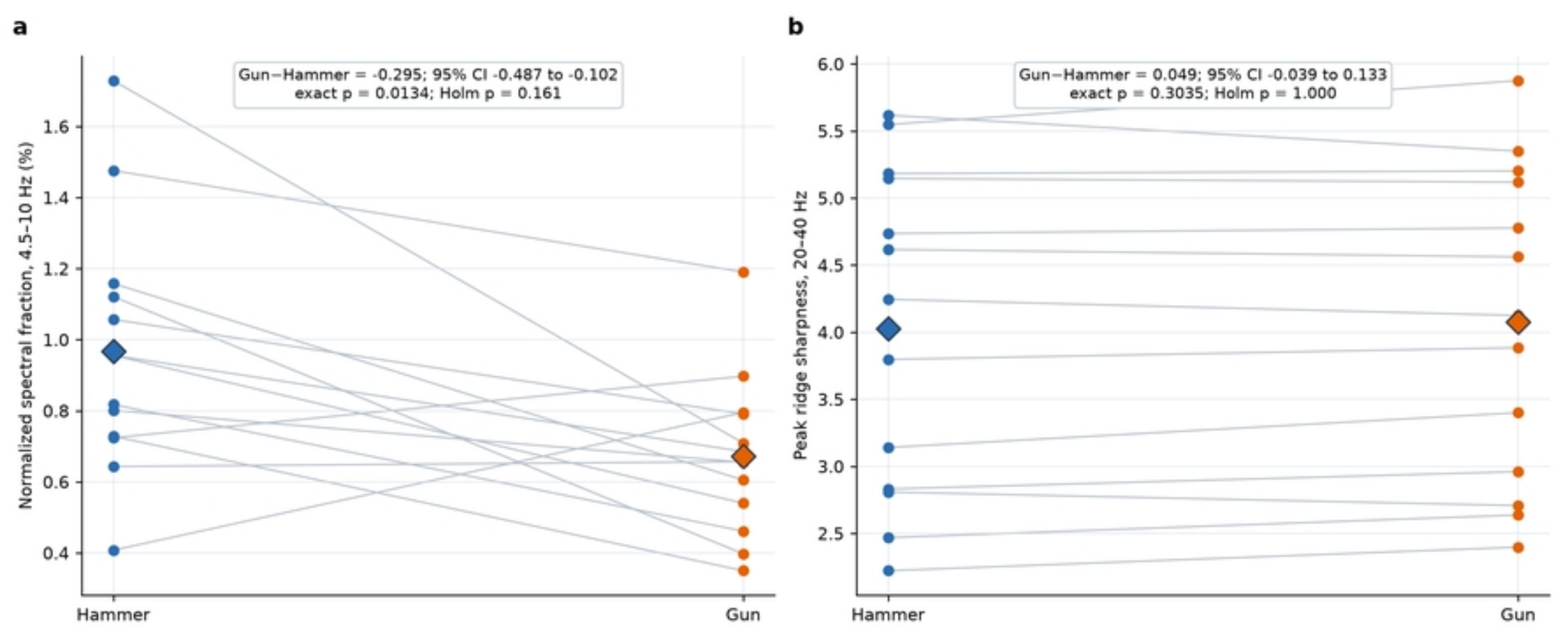
References

1. Park, C.B., Miller, R.D., Xia, J., 1999. Multichannel analysis of surface waves. Geophysics 64, 800–808. https://doi.org/10.1190/1.1444590
2. Xia, J., Miller, R.D., Park, C.B., 1999. Estimation of near-surface shear-wave velocity by inversion of Rayleigh waves. Geophysics 64, 691–700. https://doi.org/10.1190/1.1444578
3. Socco, L.V., Strobbia, C., 2004. Surface-wave method for near-surface characterization: a tutorial. Near Surface Geophysics 2, 165–185. https://doi.org/10.3997/1873-0604.2004015
4. Foti, S., Comina, C., Boiero, D., Socco, L.V., 2009. Non-uniqueness in surface-wave inversion and consequences on seismic site response analyses. Soil Dynamics and Earthquake Engineering 29, 982–993. https://doi.org/10.1016/j.soildyn.2008.11.004
5. Foti, S., Hollender, F., Garofalo, F., et al., 2018. Guidelines for the good practice of surface wave analysis: a product of the InterPACIFIC project. Bulletin of Earthquake Engineering 16, 2367–2420. https://doi.org/10.1007/s10518-017-0206-7
6. Vantassel, J.P., Cox, B.R., 2022. SWprocess: a workflow for developing robust estimates of surface wave dispersion uncertainty. Journal of Seismology 26, 731–756. https://doi.org/10.1007/s10950-021-10035-y
7. Zhang, S.X., Chan, L.S., Xia, J., 2004. The selection of field acquisition parameters for dispersion images from multichannel surface wave data. Pure and Applied Geophysics 161, 185–201. https://doi.org/10.1007/s00024-003-2428-7
8. Xu, Y., Xia, J., Miller, R.D., 2006. Quantitative estimation of minimum offset for multichannel surface-wave survey with actively exciting source. Journal of Applied Geophysics 59, 117–125. https://doi.org/10.1016/j.jappgeo.2005.08.002
9. Taipodia, J., Baglari, D., Dey, A., 2019. Effect of source characteristics on the resolution of dispersion image from active MASW survey. Indian Geotechnical Journal 49, 314–327. https://doi.org/10.1007/s40098-018-0335-1
10. Taipodia, J., Dey, A., Baglari, D., 2018. Influence of data acquisition and signal preprocessing parameters on the resolution of dispersion image from active MASW survey. Journal of Geophysics and Engineering 15, 1310–1326. https://doi.org/10.1088/1742-2140/aaaf4c
11. Wood, C.M., Cox, B.R., 2012. A comparison of MASW dispersion uncertainty and bias for impact and harmonic sources. In: GeoCongress 2012: State of the Art and Practice in Geotechnical Engineering, pp. 2756–2765. https://doi.org/10.1061/9780784412121.282

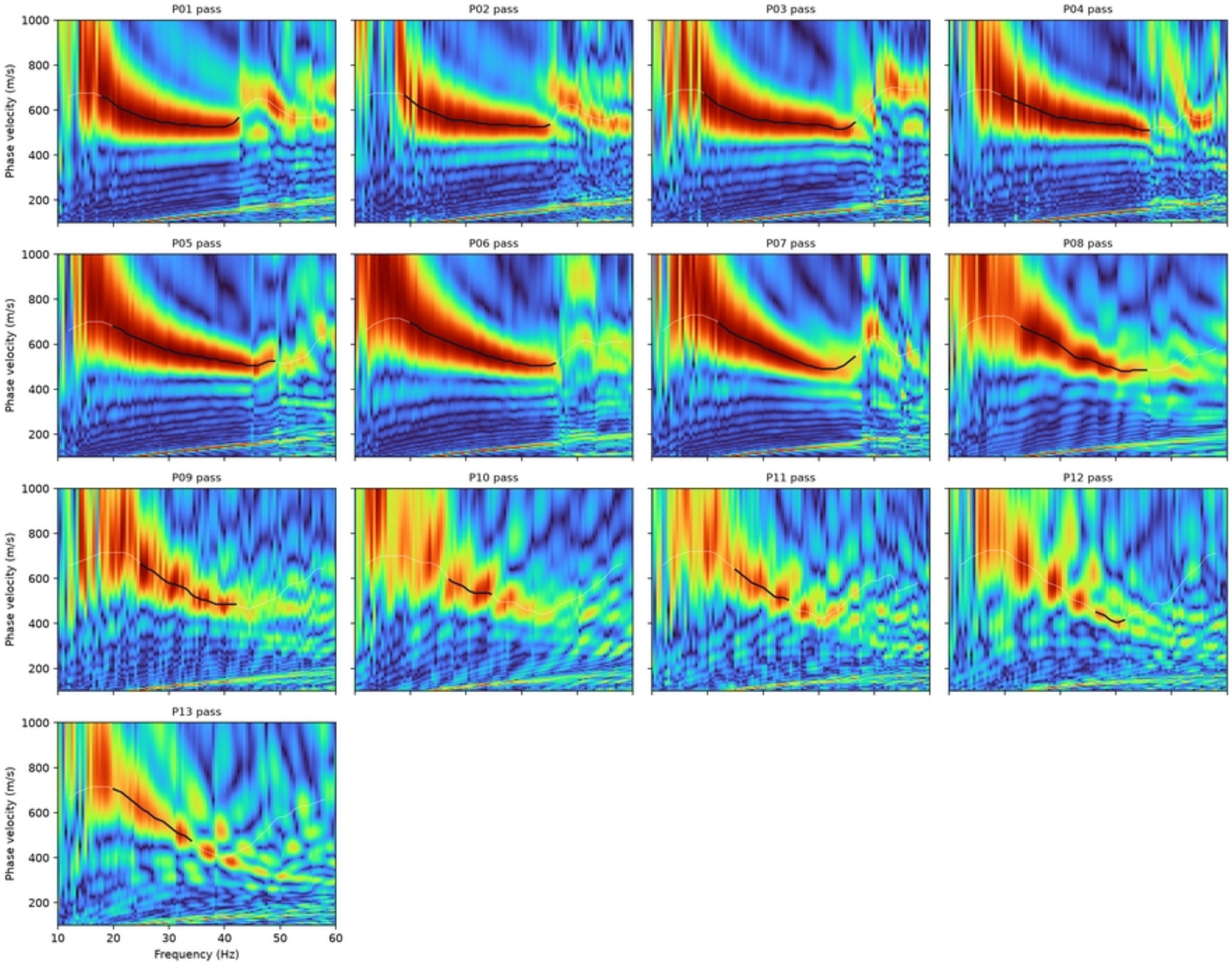
This manuscript is a preprint and has not been peer reviewed. The copyright holder has made the manuscript available under a Creative Commons Attribution 4.0 International (CC BY) license and consented to have it forwarded to EarthArXiv for public posting.

12. Cox, B.R., Teague, D.P., 2016. Layering ratios: a systematic approach to the inversion of surface wave data in the absence of a priori information. Geophysical Journal International 207, 422–438. https://doi.org/10.1093/gji/ggw282
13. Efron, B., Tibshirani, R.J., 1993. An Introduction to the Bootstrap. Chapman & Hall/CRC, New York.
14. Park, C.B., Miller, R.D., Xia, J., 1998. Imaging dispersion curves of surface waves on multi-channel record. SEG Technical Program Expanded Abstracts 1998, 1377–1380. https://doi.org/10.1190/1.1820161
15. Holm, S., 1979. A simple sequentially rejective multiple test procedure. Scandinavian Journal of Statistics 6, 65–70.
16. Efron, B., Tibshirani, R.J., 1993. An Introduction to the Bootstrap. Chapman & Hall/CRC, New York.

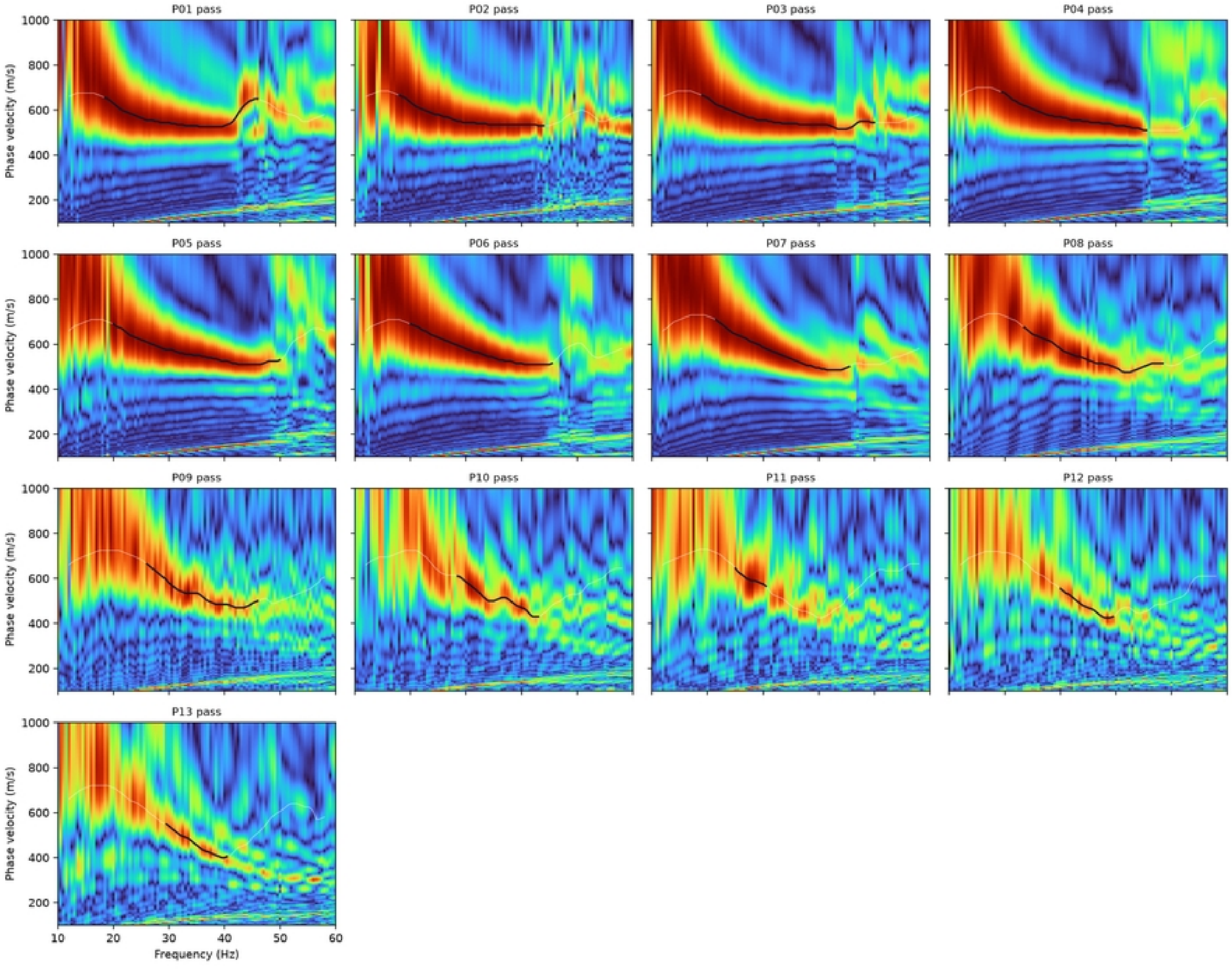

a
Matched field geometry
55 m receiver spread
30 m source offset
Hammer or gun
(same source location)
12 vertical geophones; 5 m spacing
Rolling acquisition at 13 matched locations (301-313 versus 401-413)
b
Reproducible comparison workflow
SEG-2 audit
geometry, sampling, gain, stacking
Normalized spectra
band fractions and dominant frequency
Phase-shift imaging
coherence and ridge sharpness
Dispersion QC
usable fmin, lambda max and retrieval
Paired inference
effect sizes, bootstrap CI, exact tests

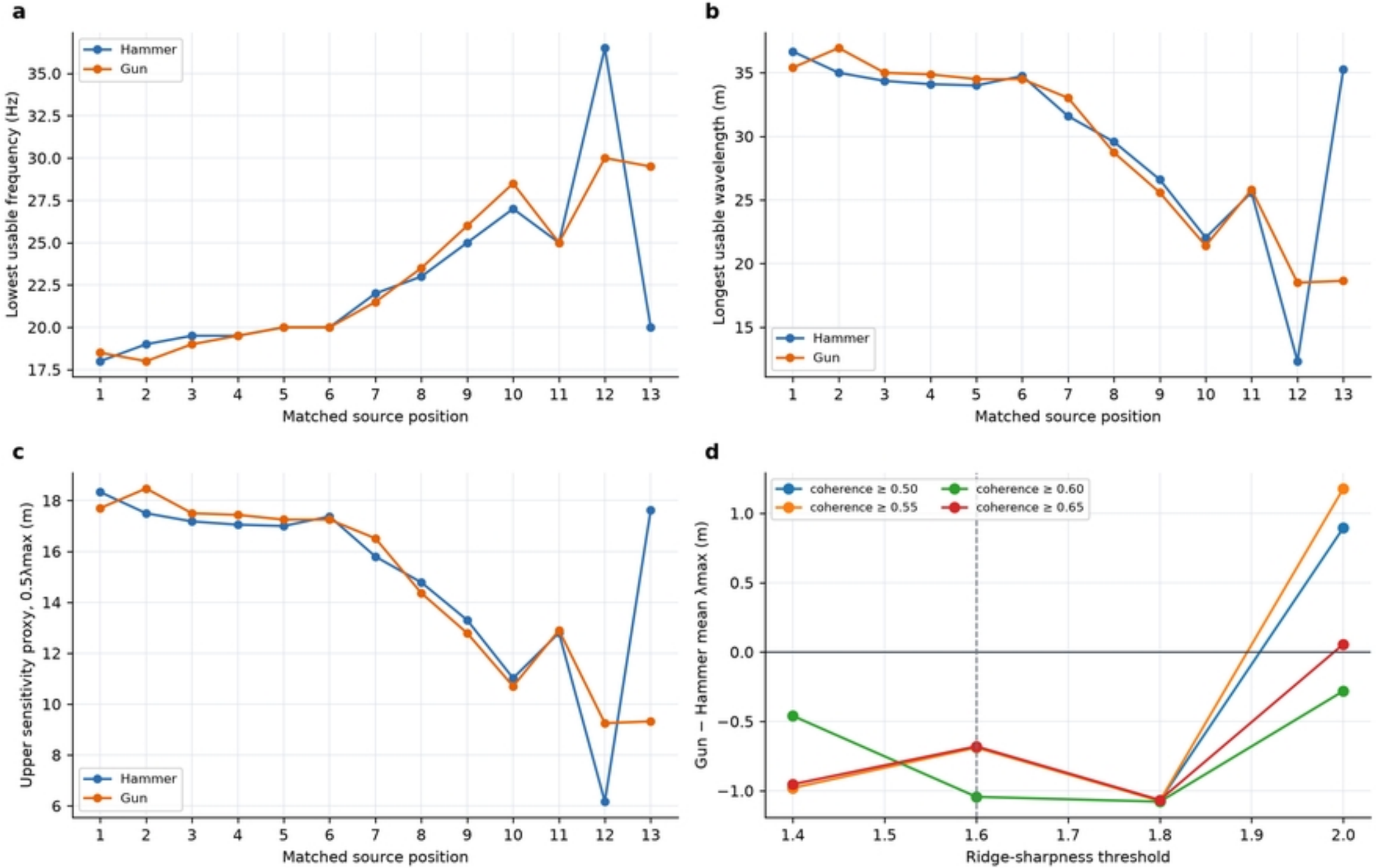

a
Gun−Hammer = -0.295; 95% CI -0.487 to -0.102
exact p = 0.0134; Holm p = 0.161
Normalized spectral fraction, 4.5–10 Hz (%)
1.6
1.4
1.2
1.0
0.8
0.6
0.4
Hammer
Gun
b
Gun−Hammer = 0.049; 95% CI -0.039 to 0.133
exact p = 0.3035; Holm p = 1.000
Peak ridge sharpness, 20–40 Hz
6.0
5.5
5.0
4.5
4.0
3.5
3.0
2.5
Hammer
Gun

Hammer: individual phase-shift images and accepted ridge segments

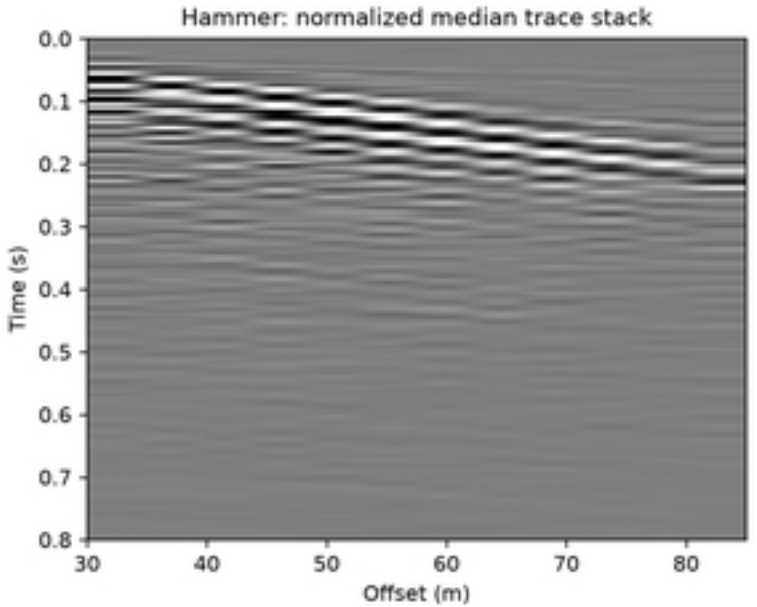


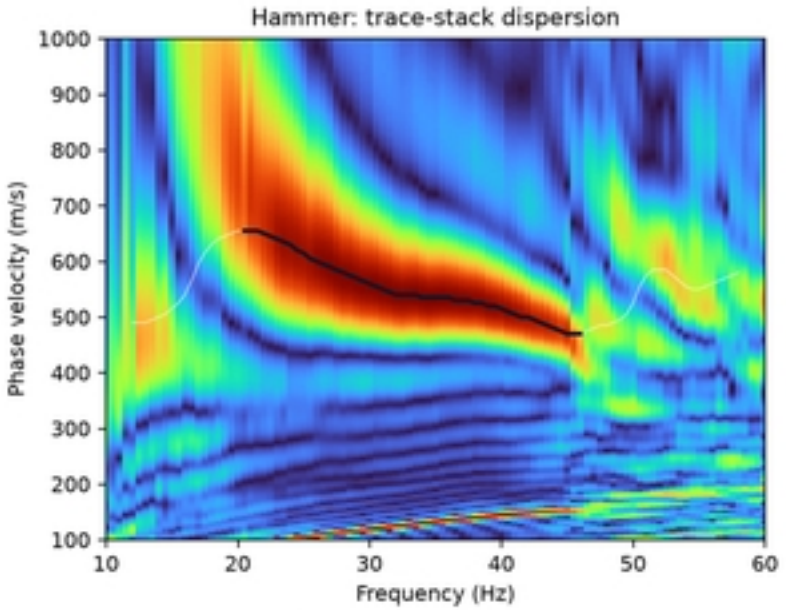
Gun: individual phase-shift images and accepted ridge segments

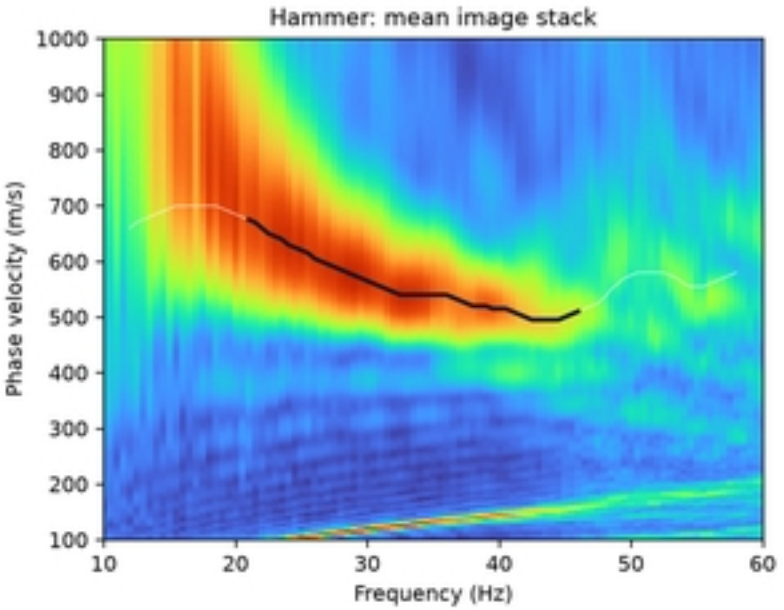


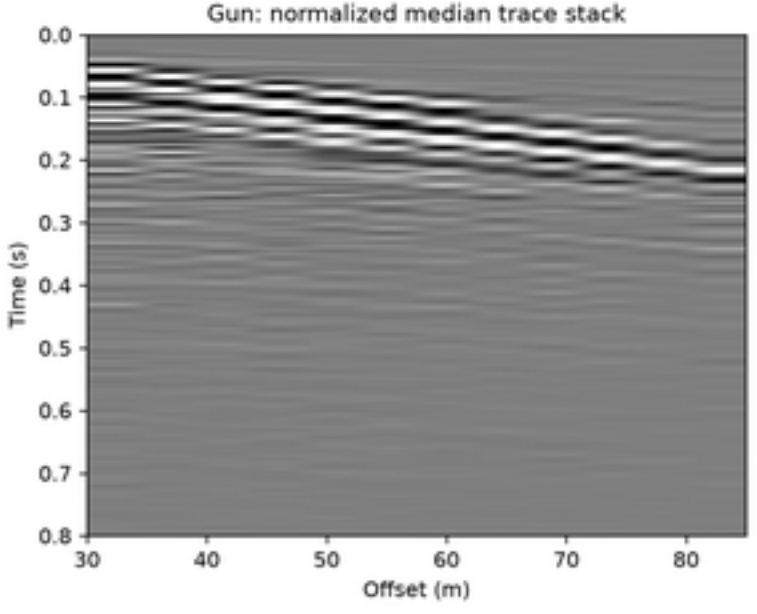

Individual dispersion usability and threshold sensitivity
a
Hammer
Gun
Lowest usable frequency (Hz)
Matched source position
b
Longest usable wavelength (m)
Matched source position
c
Upper sensitivity proxy, 0.5λmax (m)
Matched source position
d
coherence ≥ 0.50
coherence ≥ 0.55
coherence ≥ 0.60
coherence ≥ 0.65
Gun − Hammer mean λmax (m)
Ridge-sharpness threshold

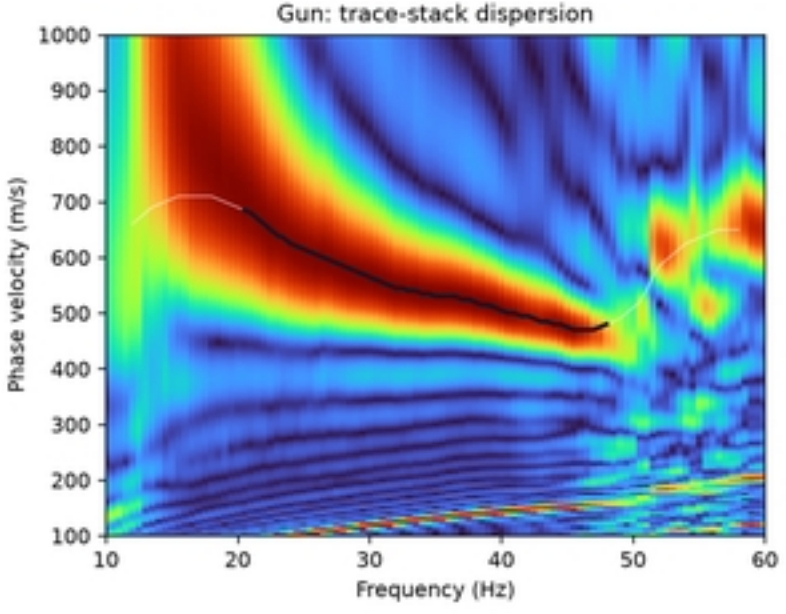
Source-composite stacks (Hammer: 13, Gun: 13)

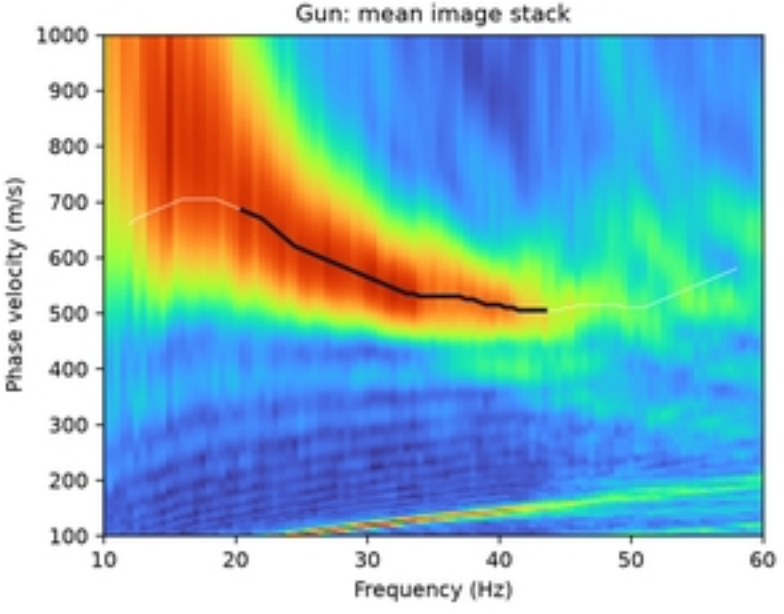


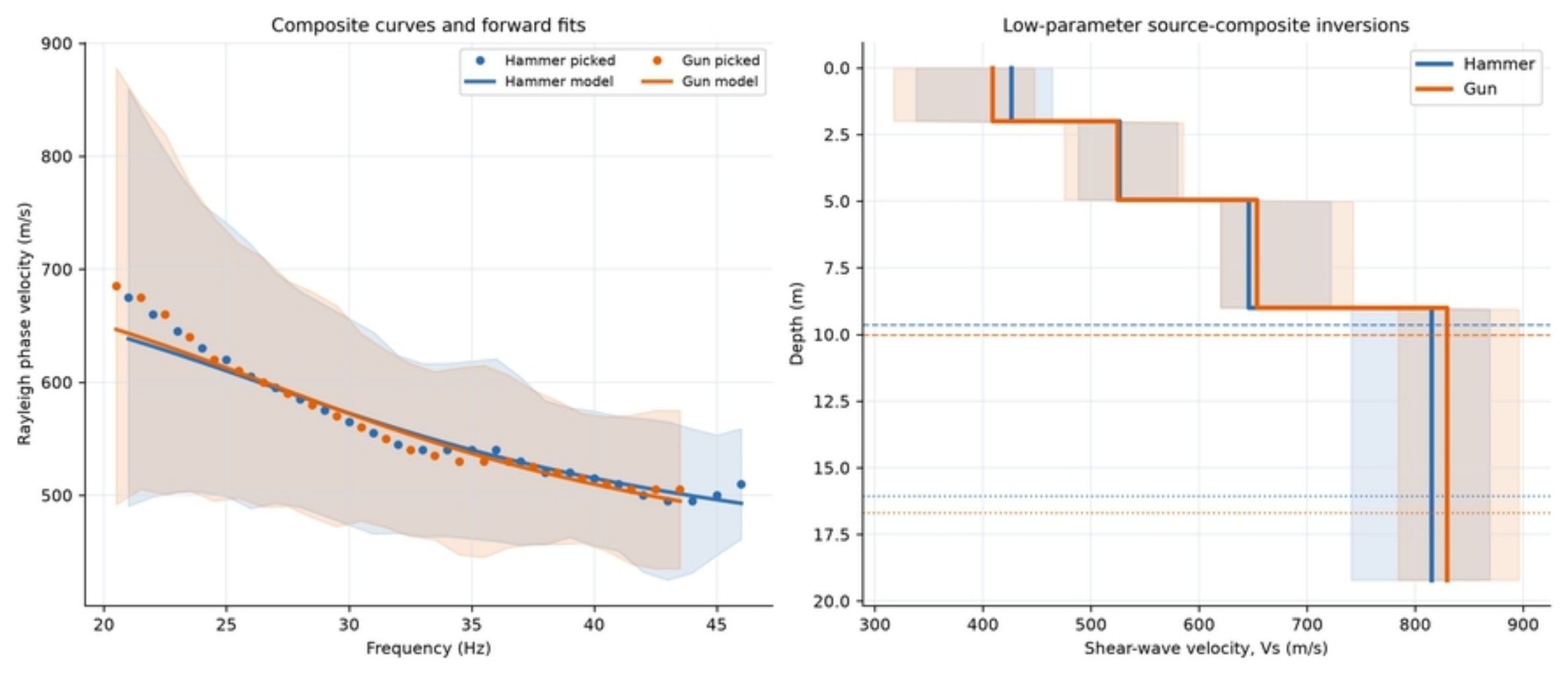


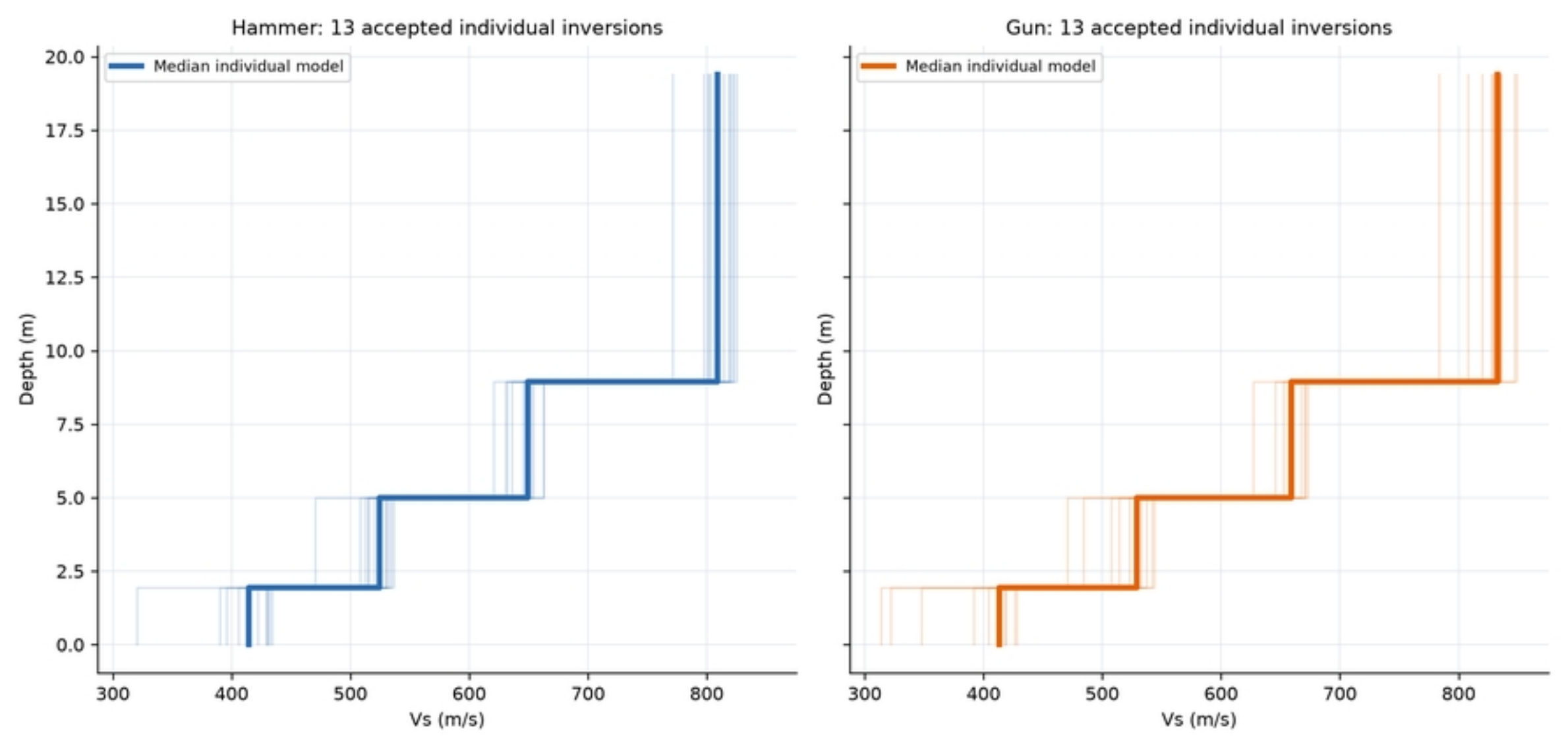









Composite curves and forward fits
Hammer picked
Gun picked
Hammer model
Gun model
Rayleigh phase velocity (m/s)
Frequency (Hz)
Low-parameter source-composite inversions
Hammer
Gun
Depth (m)
Shear-wave velocity, Vs (m/s)


Hammer: 13 accepted individual inversions
Median individual model
Depth (m)
20.0
17.5
15.0
12.5
10.0
7.5
5.0
2.5
0.0
300
400
500
600
700
800
Vs (m/s)
Gun: 13 accepted individual inversions
Median individual model
Depth (m)
300
400
500
600
700
800
Vs (m/s)